# Focusing properties of attosecond pulses

Hoflund, Maria

2021

*Document Version:*
Publisher's PDF, also known as Version of record

# Focusing properties of attosecond pulses

MARIA HOFLUND | FACULTY OF ENGINEERING | LUND UNIVERSITY

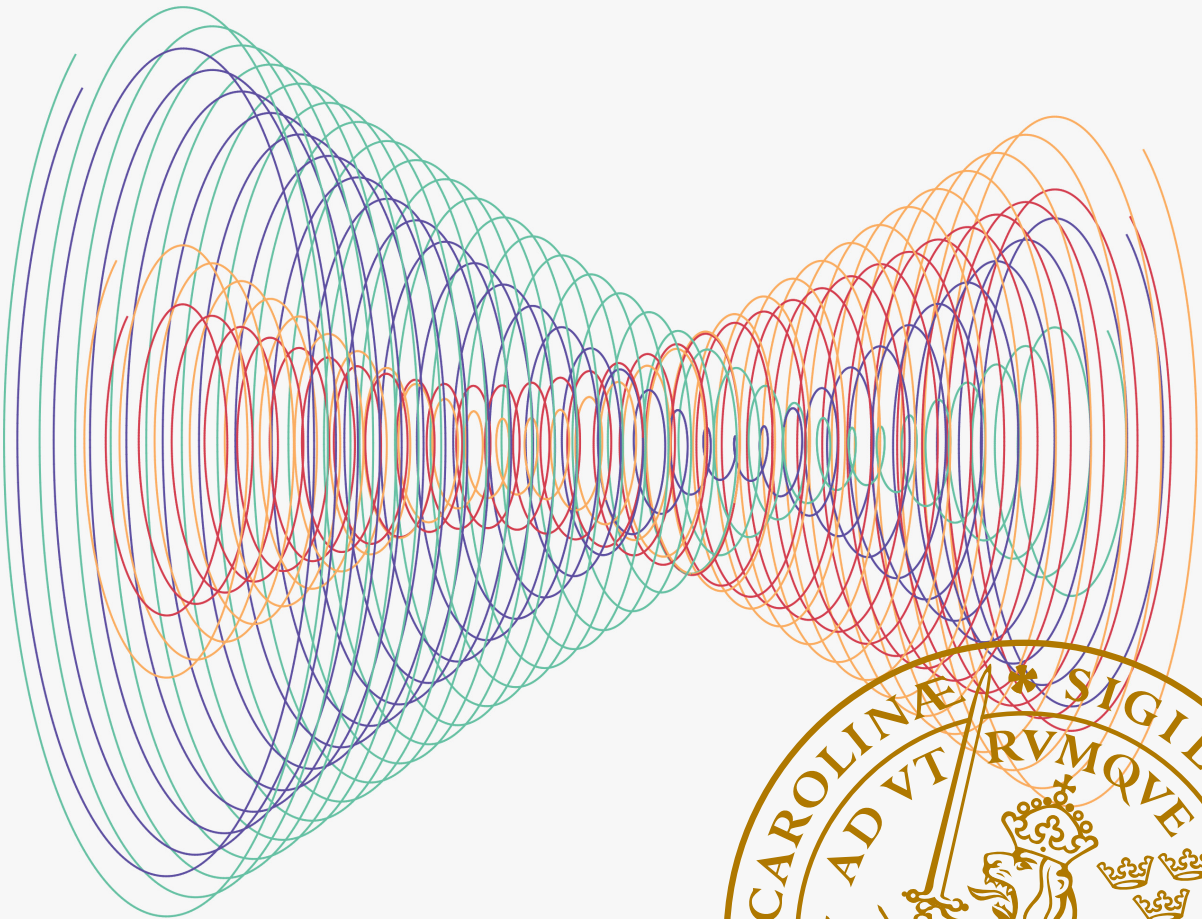

Printed by Media-Tryck, Lund 2021 NORDIC SWAN ECOLABEL 3041 0903

LUND UNIVERSITY
Faculty of Engineering, LTH
Department of Physics
Divison of Atomic Physics

ISBN: 978-91-8039-057-6 (print)
ISBN: 978-91-8039-058-3 (pdf)
ISSN 0281-2762
Lund Reports on Atomic Physics, LRAP 577 (2021)

Focusing properties of attosecond pulses

# Focusing properties of attosecond pulses

by Maria Hoflund


LUND
UNIVERSITY

Thesis for the degree of Licentiate in Engineering
Thesis advisors: Prof. Anne L'Huillier, Prof. Per Eng-Johnsson, Dr Cord Arnold
Faculty opponent: Dr Zsolt Divéki

To be presented, with the permission of the Faculty of Engineering, LTH of Lund University, for public criticism in A314 (Atomic Physics's group room) at the Department of Physics on Friday, the 26th of November 2021 at 11:00.

Organization
**LUND UNIVERSITY**
Department of Physics
Box 118
SE–221 00 LUND
Sweden

Document name
**Licentiate Thesis**

Date of disputation
2021-11-26

Sponsoring organization

Author(s)
Maria Hoflund

Title and subtitle
Focusing properties of attosecond pulses

Abstract
The discovery of high-order harmonic generation (HHG) has made it possible to see the electron dynamics on their natural time scale, attoseconds. In the HHG process, a femtosecond infrared (IR) laser pulse is converted into a train of attosecond pulses in the extreme ultraviolet (XUV), but with a very low conversion efficiency. The low intensity has to be used efficiently and that means keeping the photons compact in both space and time at the interaction with the matter you want to study.

In this thesis, the focusing properties have been measured experimentally of high-order harmonics generated in Ar using a multi terawatt laser system in a loose focusing geometry. A few micrometre focus is obtained using focusing optics with a high demagnification factor. The waist size and position of the individual harmonics have been measured using a knife-edge technique and the SWORD (spectral wavefront optical reconstruction by diffraction) technique, while varying generation parameters.

The measurements show that the harmonic focus positions are spread out along the propagation axis, which consequently decreases the peak intensity and increases the pulse duration due to the local narrowed bandwidth. However, there is a way to improve the focus by choosing the right generation parameters.

Key words
high-order harmonic generation, attosecond pulses, XUV pulses, focus optimization, knife-edge technique

Classification system and/or index terms (if any)

Supplementary bibliographical information

Language
English

ISSN and key title
0281-2762
Lund Reports on Atomic Physics, LRAP-577

ISBN
978-91-8039-057-6 (print)
978-91-8039-058-3 (pdf)

Recipient's notes

Number of pages
81

Price

Security classification

# Focusing properties of attosecond pulses

by Maria Hoflund


LUND
UNIVERSITY

A licentiate thesis at a university in Sweden takes either the form of a single, cohesive research study (monograph) or a summary of research papers (compilation thesis), which the doctoral student has written alone or together with one or several other author(s).

In the latter case the thesis consists of two parts. An introductory text puts the research work into context and summarizes the main points of the papers. Then, the research publications themselves are reproduced, together with a description of the individual contributions of the authors. The research papers may either have been already published or are manuscripts at various stages (in press, submitted, or in draft).

**Cover illustration front:** Illustration of some harmonic beams being focused, with experimentally measured properties.

**Funding information:** The thesis work was financially supported by Knut and Alice Wallenberg foundation.



Faculty of Engineering, LTH, Department of Physics

ISBN: 978-91-8039-057-6 (print)
ISBN: 978-91-8039-058-3 (pdf)
ISSN: 0281-2762
Lund Reports on Atomic Physics, LRAP-577

Printed in Sweden by Media-Tryck, Lund University, Lund 2021

# Contents

# List of publications

This thesis is based on the following publications, referred to by their Roman numerals: I, II

I **Focusing Properties of High-Order Harmonics**

**M. Hoflund**, J. Peschel, M. Plach, H. Dacasa, K. Veyrinas, E. Constant, P. Smorenburg, H. Wikmark, S. Maclot, C. Guo, C. Arnold, A. L'Huillier, P. Eng-Johnsson
*Ultrafast Science*, vol. 2021, Article ID 9797453, 8 pages, 2021

II **Complete characterization of multi-channel single photon ionization**
J. Peschel, D. Busto, M. Plach, Mattias Bertolino, **M. Hoflund**, S. Maclot, J. Vinbladh, H. Wikmark, F. Zapata, E. Lindroth, M. Gisselbrecht, J. M. Dahlström, A. L'Huillier, P. Eng-Johnsson
arXiv:2109.01581v1

# Acknowledgements

I want to say a big thank you to my main supervisor Anne L'Huillier. You have been very supportive and helpful both in my research and for me personally. Writing my first paper with you taught me a lot and I'm so impressed by your accuracy and patience. You, both as a person and your successful carrier, inspire me.

Thank you, Per. You have always made time when I've been stuck and asked for help. Talking to you makes complicated things seem clear and you always have some clever idea that I would have never had thought of. I appreciate your calmness and structure.

Thank you, Cord. I think you are a big part of the reason I started my PhD studies in the attogroup. I really enjoyed taking your courses during my master. You taught me a lot and inspired me to learn more about optics and lasers. Your curiosity inspires me.

The 10 Hz team, Jasper and Marius, it's been so fun working with you and being with you outside of work. Thank you Jasper for teaching me all kinds of things in the lab and more. I'm grateful for the time we spent both in the lab and on the sea. Thank you Marius for always being so helpful and kind. You contribute with a lot of energy and enthusiasm, which I appreciate and get impressed by. I am also happy to be boat co-owner with you. I also want to thank Hugo Dacasa for helping and supporting me when I started and felt lost and confused. And thank you Hampus Wikmark. Even though you finished before I started, you have been very helpful when I've reached out with questions.

Eric Constant, you have almost been like a supervisor to me. Thank you for all the long emails figuring out what actually happened during that campaign in November 2019 and helping me understand the mysteries of high-order harmonics. Discussing physics with you makes me happy. Speaking of the campaign, thank you Kevin Veyrinas and Peter Smorenburg for long and interesting days in the lab.

Everyone in the attogroup and the atomic physics division, thank you for making this workplace so nice.

## Popular summary in English

What are the electrons actually doing around the nucleus of an atom? That is a question we have to ask to fully understand matter, the basis of our universe. However, electrons are difficult to study due to their very fast dynamics. To be able to observe the behaviour of the electrons, we need a camera that has a higher frame rate than the speed of the electrons.

If we can understand the behaviour of electrons in atoms, we can learn to control matter in a completely new way. This could lead to all kinds of applications that we don't know of today. Just like the scientists first trying to understand electricity, we have no idea what new technology awaits us.

Since the early 2000s, we have been able to study how atoms interact with light using extremely fast, attosecond light pulses. These pulses are so short in time that you could fit 10 000 trillion of them in one second. However, there is a catch. To be able to use these short pulses, the beam, which they are travelling in, needs a nice focus where the pulses meet the atoms. If the focus is smeared out, the light intensity becomes lower and the pulse duration longer.

These light pulses are built up by several wavelength components. That means light of different colours are added up and together they form the light pulse. Characterizing the focus by using a simple knife-edge, we have found that the different wavelength components of the pulses are actually focused at different positions. Their focus positions also depend on how we generate the pulses. With this knowledge, we can pick the right generation to get the best focus.

## Populärvetenskaplig sammanfattning på svenska

Vad håller egentligen elektronerna på med runt kärnan av en atom? Det är en fråga man måste ställa sig för att fullt ut förstå materia, en av universums byggstenar. Men, elektroner är svåra att studera för att de rör sig så snabbt. För att kunna mäta deras rörelser behövs en kamera med lika hög tidsupplösning som elektronernas hastighet.

Om vi kan lära oss om egenskaerna hos elektronerna i en atom, så kan vi lära oss att kontorllera materia på ett helt ny nivå. Det skulle kunna leda till alla möjliga tillämpningar, som vi inte ens kan föreställa oss idag. Precis som de första forskarna som försökte förstå hur elektricitet fungerar, hade ingen aning vilken teknologi som har utvecklats efter det.

Sedan början på 2000-talet har vi kunnat studera hur atomer interagerar med ljus med hjälp av extremt snabba attosekundpulser. Dessa pulser är så korta i tiden att du kan rymma 10 000 trillioner av dem under en sekund. Men, det finns ett krux. För att kunna använda dessa pulser behöver strålen, som de färdas i, fokuseras väl där pulserna möter atomerna. Om fokuset är utsmetat, blir intensiteten lägre och pulslängden längre.

Dessa pulser är uppbyggda av flera våglängder. Det betyder att ljus av olika färger har adderats för att tillsammans skapa den korta pulsen. När vi karakteriserar deras fokus med ett enkelt knivsegg, ser vi att de olika våglängderna är fokuserade på olika ställen, vilket gör att fokuset blir utsmetat. Vi ser också att deras fokuspositoner är beroende av hur vi genererar ljuspulserna. Med den här kunskapen kan vi välja rätt generering för att få det bästa fokuset.

# Focusing properties of attosecond pulses

## 1 Introduction

Already around 400 BC Greek philosophers, Leucippus and Democritus, started thinking that matter consists of small uncuttable particles called atoms. It was not until the $19^{\text{th}}$ century that humanity started to understand the physics of atoms when Joseph von Fraunhofer built the first spectrometer and measured the dark lines in the spectrum of the sun ([1]). Using light as a tool revealed the energy structure of the atom. Light is still the main tool and one big challenge in atomic physics today is to resolve the fast electron dynamics that happen on the attosecond time scale.

The discovery of high-order harmonic generation (HHG) in 1987 ([2]) and 1988 ([3]) opened the door to attosecond science. The theoretical predictions were later demonstrated in 2001 ([4]) when a train of attosecond pulses was observed after focusing a femtosecond laser into a gas jet. The common method to use these pulses for time-resolved measurement is with a pump-probe method. One pulse is pumping the system, i.e. exciting or ionizing the atom, while the second pulse probes the excited system. By varying the delay between the pump and the probe, a movie of the excitation process is created. Pump-probe experiments with HHG has lead to discoveries in ionization delays in atoms ([5]; [6]), charge migrations in molecules ([7]; [8]), time-resolved inner-shell spectroscopy ([9]), and more.

The next challenge is the low conversion efficiency of HHG, which is in the order of $10^{-5} - 10^{-6}$ ([10]; [11]; [12]). This has been a limiting factor in doing pump-probe experiments with two attosecond pulses, although this has been demonstrated by some groups ([13]; [14]; [15]). The scaling principle has been a crucial component in

these successes (16). Access to high peak power laser sources enables up-scaling of the generation geometry, which means looser focusing and larger interaction volume. This principle is utilized at the intense XUV beamline in Lund, which has a focusing mirror with an 8.7 m focal length, and has done two-photon absorption experiments (17).

To achieve high intensities and keep the short pulse duration at the interaction with some gas, a small focal area is essential. That includes having all harmonics focused at the same position. This thesis is the result of Paper I, II and an experimental study of HHG by a super Gaussian IR beam. Measuring the harmonic focus positions and understanding how their focusing properties are affected by the generation process itself is the main topic of this thesis.

# 2 Theoretical background

## 2.1 Gaussian optics

The mathematical description of a laser beam is often expressed as a Gaussian beam, which is a solution to the paraxial Helmholtz equation,

$$\nabla_T^2 A - i2k\frac{\partial A}{\partial z} = 0, \tag{1}$$

where $U(r) = A(r)\exp(-ikz)$ is the complex amplitude of a paraxial wave traveling along $z$, as a function of the spatial coordinate $r = \sqrt{x^2 + y^2 + z^2}$. $A(r)$ is the slowly varying complex envelope, $k = 2\pi/\lambda$ is the wavenumber, and $\lambda$ is the wavelength. The complex amplitude of the Gaussian beam is (18)

$$U(r) = A_0\frac{w_0}{w(z)}\exp\Big[-\frac{\rho^2}{w^2(z)}\Big]\exp\Big[-ikz - ik\frac{\rho^2}{2R(z)} + i\zeta(z)\Big], \tag{2}$$

where $A_0$ is the amplitude, $w_0$ is the radius of the beam in focus and is called the waist, $\rho^2 = x^2 + y^2$ is the transverse radial coordinate, $w(z)$ is the width, $R(z)$ is the radius of curvature of the wavefront, and $\zeta(z)$ is the Gouy phase at $z$. In relation to a plane or a spherical wave, the phase between two wavefronts is not constant for a Gaussian beam, around the focus. The Gouy effect adds a phase contribution that goes from $-\pi/2$ to $\pi/2$ from $z = -\infty$ to $z = \infty$. Figure 1 illustrates some of the Gaussian beam's properties. Furthermore, the width, radius of curvature, Gouy phase, and waist are connected by the following equations:

$$w(z) = w_0\sqrt{1 + \Big(\frac{z}{z_0}\Big)^2} \tag{3a}$$

$$R(z) = z\Big[1 + \Big(\frac{z_0}{z}\Big)^2\Big] \tag{3b}$$

$$\zeta(z) = \tan^{-1}\Big(\frac{z}{z_0}\Big) \tag{3c}$$

$$w_0 = \sqrt{\frac{\lambda z_0}{\pi}}, \tag{3d}$$

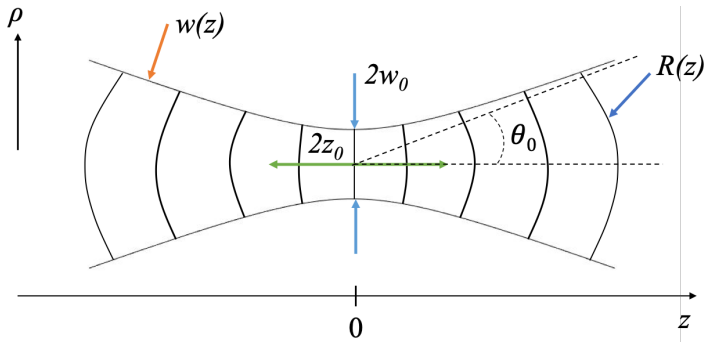


**Figure 1:** Illustration of a Gaussian beam. The waist, $w_0$, is the width of the beam in the focus, while $w(z)$ is the width at any position $z$. The Rayleigh length is the depth of focus indicated by the green arrow. The radii of curvature, $R(z)$, of the wavefronts are exaggerated to visualize the change. The dashed lines indicate the divergence angle, $\theta_0$.

where $z_0 = \pi w_0^2/\lambda$ is the Rayleigh length which describes the depth-of-focus. The divergence is the angle at which the beam is expanding with far away from the focus and can be expressed as $\theta_0 = \lambda/\pi w_0$. The waist, Rayleigh length, and divergence are all connected. If one is known the others are also known, for a given wavelength. If also the focus position is known, $w(z)$, $R(z)$, and $\zeta(z)$ can be calculated and the whole beam is defined. Alternatively, if $w(z)$ and $R(z)$ are known at a position, the position of the focus, $z$, and the beam waist, $w_0$, can be calculated by combining Equations 3(a,b,d),

$$z = \frac{R}{1 + (\lambda R/\pi w^2)^2} \tag{4a}$$

$$w_0 = \frac{W}{\sqrt{1 + (\pi w^2/\lambda R)^2}}. \tag{4b}$$

This is used later to derive the focus positions and waist of the harmonics by knowing the width and radius of curvature at the generation.

### Beam quality factor

In reality, there are no perfect Gaussian beams. One way to still use this mathematical description is to use it with a beam quality factor, $\mathbb{M}^2$. For a beam with a waist $w_m$ and divergence $\theta_m$ the quality factor is defined by the ratio to an ideal Gaussian beam

$$\mathbb{M}^2 = \frac{w_m \theta_m}{w_0 \theta_0} = \frac{w_m \theta_m}{\lambda/\pi}. \tag{5}$$

The beam quality factor is never below one, which means that for a given beam waist the divergence angle for a non-ideal Gaussian beam is always larger than the ideal Gaussian beam.

### Focusing a Gaussian beam

What a focusing element is effectively doing to light is to introduce a radial dependent phase that modulates the wavefront. A focusing element, with a focal length $f$, changes the radius of curvature of the Gaussian beam $R$ to $R'$ and width $W$ to $W'$ as follows

$$\frac{1}{R'} = \frac{1}{R} - \frac{1}{f} \tag{6a}$$

$$W' = W. \tag{6b}$$

Using Equation 6 together with the relations in Equation 3, the following parameter transformations can be derived as shown in B.E.A. Saleh and M.C. Teich ([18]),

$$w_0' = M w_0 \tag{7a}$$

$$(z' - f) = M^2 (z - f) \tag{7b}$$

$$z_0' = M^2 z_0 \tag{7c}$$

$$\theta_0' = \frac{\theta_0}{M}, \tag{7d}$$

where,

$$M = \frac{M_r}{\sqrt{1+r^2}} \tag{8a}$$

$$r = \frac{z_0}{z-f} \tag{8b}$$

$$M_r = \left|\frac{f}{z-f}\right|. \tag{8c}$$

Generally, this is very similar to the lens imaging equation of geometrical optics. The only difference is that the magnification factor, $M$, is wavelength dependent, due to the Rayleigh length ($z_0$) in Equation 8b.

## 2.2 High-order harmonic generation

High-order harmonic generation (HHG) is a highly nonlinear process where a fundamental pulse is converted into a train of pulses built up by odd multiples (harmonics) of the fundamental frequency. This has enabled the breakthrough of generating the shortest light pulses ever.

The duration of a light pulse is limited by the period of the oscillation electric field. The pulse can never be shorter than one oscillation. Generating an ultrashort pulse, therefore, needs a high carrier frequency. Pulse duration on the attosecond timescale cannot be created with a normal laser, due to the spectral limitations of the gain medium. Through the high-order harmonic process, the carrier frequency can be 15-20 times higher than the fundamental frequency and creates a very broad spectrum. This combination enables a pulse duration on the order of 100 as.

### Three step model

High-order harmonics are generated by focusing an intense pulsed laser beam into a noble gas. The interaction between the light and the gas can be described with the three step model ([19; 20]) and is illustrated in Figure 2. If the amplitude of the electric field of the laser is comparable with the Coulomb potential of the atom, the potential will be distorted. An electron can then tunnel through the potential barrier and the first step has happened: tunnel ionization. In the second step, the free electron is accelerated away and then back to the atom

by the electric field of the laser, while it is changing sign. Back at the parent ion, the electron can recombine with the atom and then a high energy photon (usually in the XUV range) is emitted, and that is the third and last step.

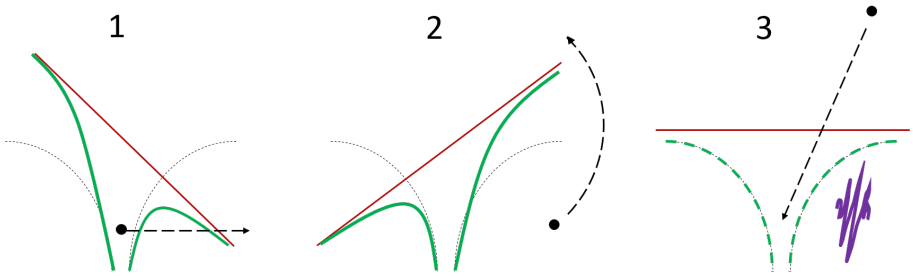


**Figure 2:** Illustration of the three step model. First, the electron leaves the atom by tunnel ionization. Second, the electron is accelerated in the electric field of the laser. Third, the electron recombines and an XUV photon is emitted.

### Classical description of the electron propagation

To understand some crucial features of HHG, a classical description can be used to describe the electron's trajectory in the electric field. Assuming that the electron has zero velocity right after ionization and that it only experiences the force of the laser field, i.e. the Coulomb force is negligible, Newton's second law can be used to derive its trajectory,

$$\ddot{x}(t) = \frac{-e}{m_e} E_0 \cos\omega_0 t \tag{9a}$$

$$\dot{x}(t) = \frac{-eE_0}{m_e\omega_0}\big[\sin\omega_0 t - \sin\omega_0 t_0\big] \tag{9b}$$

$$x(t) = \frac{eE_0}{m_e\omega_0^2}\big[\cos\omega_0 t - \cos\omega_0 t_0 + \omega_0(t-t_0)\sin\omega_0 t_0\big], \tag{9c}$$

where $\omega_0$ is the angular frequency of the driving laser, $t_0$ is the time at which the electron is free from the atom, $E_0$ is the amplitude of the electric field, and $e$ and $m_e$ are the charge and mass of the electron. The electron can be released at different times, $t_0$, in the optical cycle. By putting $x(t) = 0$ and solving the equation numerically, the trajectories that return to the atom can be found, as well as the return times. Using the velocity at the return time, the kinetic energy can be found and is given by

$$E_{kin} = 2U_p\big[\sin\omega_0 t_r - \sin\omega_0 t_0\big]^2, \tag{10}$$

where $U_p$ is the ponderomotive energy and is equal to $e^2E_0^2/4m_e\omega_0^2$. The sum of the kinetic energy and the potential energy is the energy of the emitted photon.

The emitted photon energy as a function of return time in argon is plotted in Figure 3, for a peak intensity of $1.5 \times 10^{14}$ W/cm$^2$ and wavelength of 800 nm. The trajectories are categorised into two groups: short (blue) and long (red). There is one trajectory right in between that gives the maximum photon energy. This is also called the cut-off energy and is proportional to the ponderomotive energy as $3.17U_p$.

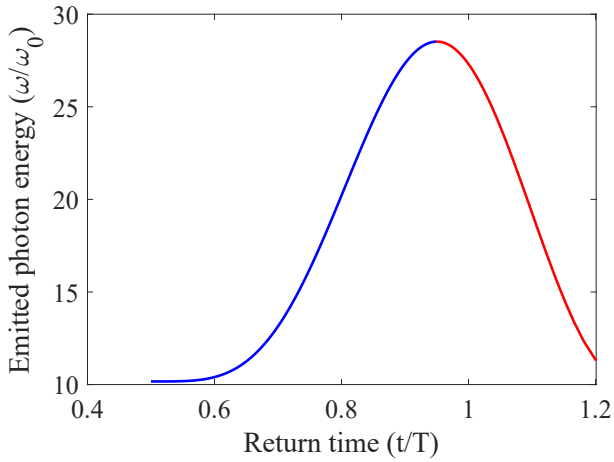


**Figure 3:** Numerical calculation of the emitted photon energy as a function of return time of the electron. The blue curve represents the short trajectory and red the long. It is calculated for a driving laser centered at $\omega_0$, period $T$, and peak intensity of $1.5 \times 10^{14}$ W/cm$^2$ interacting with argon.

The three step process repeats every half cycle of the driving laser. Therefore, a train of pulses is generated. These pulses interfere so that the spectrum becomes a comb of odd harmonics of the driving laser's frequency.

## 2.3 Model for HHG focus

The Gaussian beam has a transverse radial dependent intensity and that has implications on the properties of the generated harmonics. As shown in Equation 9, the trajectories depend on the amplitude of the driving field, $E_0$. This, in turn, affects the return time and photon energy. Since photons of different energies are emitted at different times, this will affect the phase of the XUV radiation. This phase is called the dipole phase (21) and to understand its behaviour, an analytical expression has been developed by Guo et.al. (22) and Wikmark et.al. (23), and will be derived here.

Starting from the emitted photon energy as a function of return time, as shown in Figure 3, the curve is approximated by two tangents: one for the short trajectory and one for the long. Calling the minimum angular frequency $\Omega_p$, which corresponds to the potential energy, and the maximum $\Omega_c$, corresponding to the cut-off energy, the tangents are taken at $(\Omega_c + \Omega_p)/2$. The return times where the tangents reach $\Omega_p$ and $\Omega_c$ are called $t_{pi}$ and $t_{ci}$, where $i$ refers to the two trajectories ($s$ and $l$). These times are intensity independent. The approximated analytical expression for the harmonic angular frequency, $\Omega$, as a function of return time, $t$, is then

$$\Omega(t) \approx \Omega_p + \frac{\Omega_c - \Omega_p}{t_{ci} - t_{pi}}(t - t_p), \tag{11}$$

and the inverse function, i.e. return time in terms of $\Omega$, is given by

$$t(\Omega) \approx t_{pi} + \frac{t_{ci} - t_{pi}}{\Omega_c - \Omega_p}(\Omega - \Omega_p). \tag{12}$$

The spectral phase $\Phi(\Omega)$ is given by the integral of $t(\Omega)$,

$$\Phi_i(\Omega) = \Phi_i(\Omega_p) + t_{pi}(\Omega - \Omega_p) + \frac{t_{ci} - t_{pi}}{\Omega_c - \Omega_p}\frac{(\Omega - \Omega_p)^2}{2}. \tag{13}$$

This expression can be written in a more compact form by introducing the constant $\gamma_i$ as

$$\gamma_i = \frac{(t_{ci} - t_{pi})\pi c^2 m_e}{3.17\alpha_{FS}\lambda^2}, \tag{14}$$

where $\alpha_{FS}$ is the fine structure constant and $\lambda$ is the wavelength of the fundamental beam. Furthermore, the constant term in the spectral phase, $\Phi_i(\Omega_p)$, is zero for the short trajectory and proportional to the intensity for the long trajectory. It can be replaced by $\Phi_i(\Omega_p) = \alpha_i I$, where $\alpha_s = 0$ and $\alpha_l$ can be found numerically from the classical description, i.e. the curve in Figure 3. Inserting $\gamma_i$ and $\alpha_i$ into Equation 13, the spectral phase can be written as

$$\Phi(\Omega) = \alpha_i I + t_{pi}(\Omega - \Omega_p) + \frac{\gamma_i}{I}(\Omega - \Omega_p)^2. \tag{15}$$

This equation shows clearly the intensity dependence in the dipole phase. It turns out that the radial dependent intensity results in a radial dependent phase which modifies the curvature of the wavefront. As a consequence, all harmonics cannot be focused on the same position. This affects both the peak intensity and the pulse duration.

To calculate the harmonic focus positions and waist size, the next step is to introduce the Gaussian beam and calculate the radius of curvature for the harmonics. The phase of the harmonics has two contributions: the phase of the fundamental multiplied by the harmonic order and the dipole phase. Assuming that the generation process is dominated by one trajectory the harmonic phase of order $q$ can be approximated by

$$\Phi_q(\rho, z) = q\phi(\rho, z) + \Phi_i(\rho, z), \tag{16}$$

where $\phi(\rho, z)$ is the phase of the fundamental beam and is given by the last factor in Equation 2.

The Gaussian intensity is the absolute square of the complex amplitude given in Equation 2. Inserting the Gaussian intensity in Equation 15 and only considering the radial dependent terms, the dipole phase can be expressed as

$$\Phi_i(\rho, z) = \frac{\alpha_i I_0 w_0^2}{w^2(z)} e^{-\frac{2\rho^2}{w^2(z)}} + \frac{\gamma_i(\Omega - \Omega_p)^2 w^2(z)}{I_0 w_0^2} e^{\frac{2\rho^2}{w^2(z)}}, \tag{17}$$

where $I_0 = |A_0|^2$. The exponential terms are expanded in a Taylor series, $\exp[-2\rho^2/w^2(z)] \approx 1 - 2\rho^2/w^2(z)$, and only the radial dependent term is kept. The $\rho^2$-dependent phase contribution to $\Phi_q(\rho, z)$ is

$$\frac{qk\rho^2}{2R(z)} - \frac{\alpha_i I_0 w_0^2}{w^2(z)} \frac{2\rho^2}{w^2(z)} + \frac{\gamma_i(\Omega - \Omega_p)^2 w^2(z)}{I_0 w_0^2} \frac{2\rho^2}{w^2(z)}. \tag{18}$$

The radius of curvature is found by comparing this equation to the $\rho^2$-dependent phase for a Gaussian beam, $qk\rho^2/2R_i(z)$, and is given by

$$\frac{1}{R_i(z)} = \frac{1}{R(z)} - \frac{4\alpha_i I_0 w_0^2 c}{w^4(z)\Omega} + \frac{4\gamma_i(\Omega - \Omega_p)^2 c}{I_0 w_0^2 \Omega}, \tag{19}$$

where c is the speed of light.

To determine the focus position of the harmonics, the width at the generation position is also needed. A simple way to estimate it is to assume that the harmonic amplitude is proportional to the fundamental amplitude to the power of $p$ ([24; 25; 26; 27; 28]). With time-dependent Schrödinger equation (TDSE) calculations, the proportionality factor is found to be equal to 4 ([23]). The harmonic width is then simply half the width of the fundamental, $W(z) = W_{IR}(z)/2$. Inserting $R_i(z)$ and $W(z)$ into Equation 4a and 4b, the focus position ($z_{qi}$) and waist size ($w_{0,qi}$) of each harmonic can be found.

# 3 Experimental setup and method

The experiments conducted in this thesis have been performed at the intense XUV beamline which is part of the Lund High-Power Facility at the Lund Laser Centre (LLC). The beamline includes several main sections: the terawatt laser system, pulse preparation, HHG, interferometer, and diagnostics and application. The terawatt laser is placed in a separate room and is also used for other experiments, e.g. laser wakefield acceleration.

## 3.1 The terawatt laser

The terawatt laser system is based on a passively mode-locked Ti:Sapphire laser oscillator. It has a central wavelength of 800 nm and a repetition rate of 80 MHz, which is later reduced to 10 Hz by a pulse picker. Before the pulses are going through the chirped pulse amplification (CPA) process they are pre-amplified and the spectral phase is modified with an acousto-optical modulator.

The CPA process was developed in the '80s and led to a breakthrough in the generation of high peak power laser pulses (29). When amplifying a laser pulse there is always a limit to what power the amplification crystal and other optics can handle without being damaged. To tackle this problem, the pulses are first stretched by introducing a chirp. A chirped pulse has a varying instantaneous frequency, which makes the pulse duration longer. The energy of the stretched pulse is distributed over a longer period in time and therefore has a lower peak intensity. This means that it can be amplified without damaging any optics. After the amplification, the pulse is compressed again by removing the chirp, resulting in high peak power (e.g. in the terawatt range).

In the terawatt laser system, frequency-doubled high-energy Nd:YAG lasers are used to pump a Ti:Sapphire crystal in a regenerative amplification scheme. The pulses pass the crystal 20-30 times before they are ejected by a Pockels cell. Lastly, a final amplification is done in a five-pass butterfly amplifier, also using a Ti:Sapphire crystal. At this stage, the pulses have an energy of 400 mJ and a bandwidth of 37 nm. Before compression, the beam is divided into two paths: one for further amplification to be used for laser-driven acceleration and the other for the intense XUV beamline.

## 3.2 Pulse preparation

### Attenuator

The pulse energy in the beamline is controlled by an attenuator, composed of a motorized half-wave plate and a polarizer. The half-wave plate is a birefringent crystal that rotates the linearly polarized light of the incoming beam by $2\theta$, where $\theta$ is the angle between the polarization of the incoming light and the orientation of the ordinary axis in the crystal. After the half-wave plate, there is a polarizer, which only transmits horizontally polarized light. Depending on the orientation of the polarization after the half-wave plate ($2\theta$) the output intensity is $I_{att} = \cos^2(2\theta)$.

Before the beam goes into vacuum it is expanded by a telescope to increase the beam diameter to 38 mm. The beam is then guided through transport tubes to the next room where the intense XUV beamline starts. The vacuum is in the order of $10^{-6}$ mbar and is used to reduce nonlinear effects and other disturbances from the air such as temperature and airflow. A sketch of the whole beamline is shown in Figure 4.

### Grating compressor

In vacuum, the beam is compressed by a grating compressor. It consists of two gratings and a retroreflecting mirror (labeled grat. 1, 2, and retro in Figure 4). The pulse is dispersed by the first grating making the path length to the next grating wavelength dependent. The second grating makes all wavelength components go straight to the retroreflector which changes the beam height and then the beam goes back. The wavelength-dependent path length difference results in a compressed pulse where all wavelength components are overlapped in time.

The amount of chirp introduced by the grating compressor is controlled by varying the distance between the two gratings. The right position is found by measuring the pulse duration while varying the distance. The pulse duration is measured with a single shot autocorrelator (Bonzai from Amplitude Technologies). It splits the beam in two parts and overlaps them in a second harmonic crystal with a small angle between the two beams. The second harmonic signal is detected with a camera and the pulse duration is determined from the width of this signal.

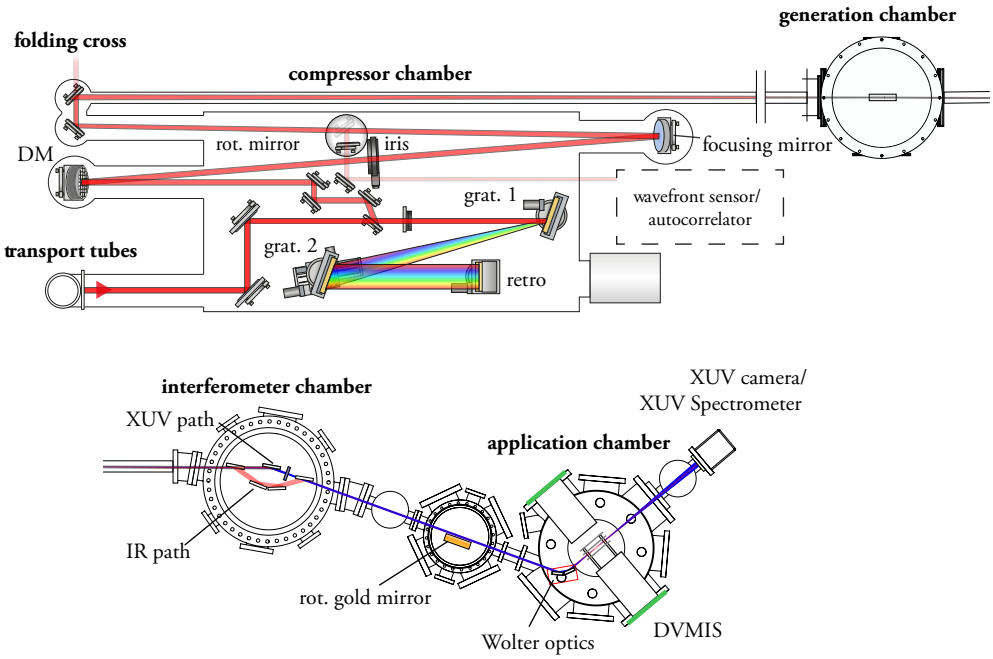


**Figure 4:** Overview of the intense XUV beamline split in two parts. The beam comes in from the transport tubes and goes into the grating compressor (grat. 1, 2, and retro). The wavefront is then corrected by the deformable mirror (DM) and goes through an iris to the focusing mirror. The beam is folded and then focused in the generation chamber. After generation, the XUV and IR are split in the interferometer. The beam can be analysed by inserting a rotatable golden mirror or sent straight to the application chamber. There it is focused by the Wolter optics and the DVMIS, XUV camera or the spectrometer can be used. The compressor chamber also has a rotatable mirror that can take out the beam to the wavefront sensor or the autocorrelator.

## Wavefront correction and focusing

To optimize the wavefront quality, aberrations are reduced by a deformable mirror (DM). The area of the mirror is divided into 31 sections where each one of them is controlled by a piezoelectric actuator. In addition, there is a piezo disc that controls the general curvature of the mirror, introducing a convergent or divergent wavefront to the beam. The DM corrects the wavefront in a closed-loop by measuring the wavefront with a Shack-Hartmann sensor and using an optimization algorithm.

The Shack-Hartmann sensor consists of a microlens array and a camera ([30]). Each lens probes one small section of the wavefront and focuses the light. If the wavefront is not flat, the focus will be displaced. Recording the displacement for each lens, the wavefront of the whole beam can be reconstructed.

Some practical things that have to be considered in this closed-loop system are

that the beam has to be well aligned in the centre of the deformable mirror. If not, the overall curvature control will misalign the beam. Another thing is that to be able to use the wavefront sensor, the beam surface of the DM has to be imaged onto the sensor. It is important to have a well-aligned lens doing that so that this lens does not introduce aberrations.

After the deformable mirror, there is a motorized iris and then the beam is loosely focused by a spherical mirror with a focal length of 8.7 m. By changing the piezo disc on the DM, the focal position can be varied, having the IR focus before or after the generation gas.

### 3.3 High-order harmonic generation

A pulsed gas valve is used to inject the generation gas. A triggered voltage pulse opens the valve for a certain amount of time. The pulse length, delay, and peak value are controllable. The valve can generate a jet or a cell can be mounted on the valve. The 1 cm gas cell used during this thesis's work is essentially a metallic cylindrical tube with open ends. Different noble gases can be connected to the valve. Argon was used in the experiments described in Paper I and II. The local pressure in the gas cell cannot be measured in the current setup but is in general in the mbar regime for HHG.

### 3.4 Interferometer

An important application of the intense XUV beamline is to do pump-probe experiments, both with XUV-IR but also with XUV-XUV. A Mach-Zehnder interferometer has been designed (31) that can do both types. A sketch of the setup is shown in Figure 5. First, the XUV and IR beams are split up by a holey mirror, where the XUV goes through and the IR is reflected. This is possible since high-order harmonics generally have lower divergence than the driving laser, due to their shorter wavelengths.

The XUV beam (marked in blue in Figure 5) is reflected by a split-and-delay unit (SDU) (33). This is built up by two silica plates which split the beam spatially into two parts. By moving the second plate, a delay between the beams can be introduced. The silica plates are anti-reflective coated for the IR to minimize its reflectance. The rest of the IR in the XUV beam path is filtered out by a thin film of aluminium placed after the SDU.

The IR beam (marked in red in Figure 5) goes through a half-wave plate and is

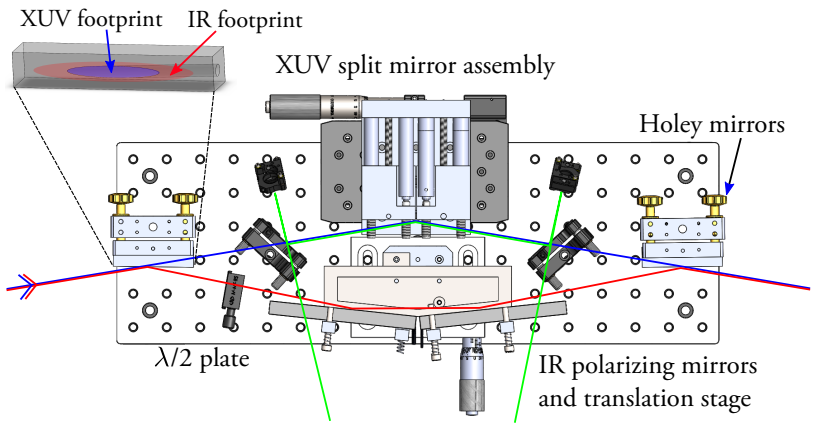


**Figure 5:** Sketch of the interferometer setup design. The IR (red) and XUV (blue) are split up by the first holey mirror. The XUV is reflected by the split and delay unit, while the IR is reflected on two glass plates on a delay stage after going through a rotatable half-wave plate. A green diode laser (green) is overlapped with the XUV at the split and delay unit and is used for active stabilization of both alignment and delay. The figure is taken, with permission, from H. Wikmark's PhD thesis (32).

then reflected twice by multilayer-coated glass plates mounted on a delay stage. This coating acts as a polarizer and the transmitted IR intensity can therefore be controlled by rotating the half-wave plate. Before the IR and XUV beam are recombined with a second holey mirror, the IR goes through a motorized iris (not shown in Figure 5) to enable further attenuation.

To achieve high precision both spatially and temporally when using the SDU, a stabilizing feedback loop is used. Having two more holey mirrors in the XUV beam path, a green diode laser (marked in green in Figure 5) is coupled in to co-propagate with the XUV while being reflected by the SDU. The diode laser has two parallel beams that are reflected on one silica plate each. They are then combined outside the chamber to measure the temporal and spatial overlap at a distance corresponding to the focus of the XUV. A PID-loop is used to control the delay and alignment of the second silica plate (33).

The delay stage in the IR arm is moved by piezoelectric actuators. It has a delay range of 560 fs and a resolution of 30 as while the SDU has a range of 50 fs and a resolution of 20 as (32).

## 3.5 Diagnostics and Application

The last vacuum chamber of the beamline is called the application chamber. This is where the beam is focused and can be overlapped with a pulsed gas jet

that is injected by an Even-Lavie valve (34). This chamber also has several diagnostics tools: XUV spectrometer, XUV camera, photodiode, Hartmann mask, and a double-sided velocity map imaging spectrometer (DVMIS).

### Focusing optics

Focusing broadband XUV radiation is not trivial. A lens cannot be used due to strong absorption in this wavelength region. A spherical mirror is also problematic since it requires almost normal incidence. Due to the fact that XUV radiation has a refractive index close to 1 for most materials, there is very low reflectivity at normal incidence. The solution is then to have a small grazing incidence angle. Using two toroidal mirrors is a way to reduce aberrations in a practical manner.

H. Coudert-Alteirac et al. (35) describe the implementation and characterization of a Wolter-like configuration of two toroidal mirrors installed in the intense XUV beamline. These optics are placed 6 m after the generation gas, with an image 170 mm down the line, resulting in a demagnification of 35. Using a Hartmann mask (36), the focus size was determined to be 3.6 x 4.0 $\mu m^2$ full width at half maximum (FWHM).

### Spectrometer

The XUV spectrometer includes an aberration-corrected concave grating, a multichannel plate (MCP), a phosphor screen, and a camera. The grating is placed on a movable mount so that it can be inserted in or removed from the beam path enabling the measurement of the spectrum or letting the beam go straight to an XUV camera. The grating is concave so that it images the XUV focus in the vertical direction, which acts as an entrance slit. The aberration correction makes the spectrum imaged onto a flat field instead of a sphere. The horizontal axis is just reflected by the grating, which makes the information about the beam width preserved along this axis. The dispersed beam hits the MCP which amplifies the signal that is converted by a phosphor screen and finally detected by a camera.

### Double-sided Velocity Map Imaging Spectrometer

To study the attosecond pulse train interaction with matter, a double-sided velocity map imaging spectrometer is used. In the XUV focus, the light is

overlapped with a pulsed supersonic gas jet generated with an Even-Lavie valve ([34]) and two skimmers. The DVMIS detects the products of the photo-induced ionization process by applying an electric field that makes the electrons and ions go in opposite directions towards two different MCP:s. The electric field is generated by electrodes and by applying different voltages to the electrodes different measurement modes can be used.

The velocity map imaging mode maps the momentum of the particles on the MCP. The 3D momentum distribution is projected onto the 2D MCP. The cylindrical symmetry around the linear polarization axis enables the 3D momentum distribution to be reconstructed through Abel transform from the 2D projection ([37]).

# 4 Chromatic aberration of HHG

Chromatic aberration in the HHG focus has been demonstrated before, using interference (38) or diffraction techniques (39; 40; 41) to measure the individual harmonic wavefronts and from that retrieve the harmonic focus positions. This chapter goes through two experiments performed at the intense XUV beamline to measure the focusing properties of HHG. The first one uses a knife-edge technique to investigate the focusing properties for different generation positions. The experimental results are compared with simulations based on the model described in section 2.3. The results of this experiment are published in Paper I. The second experiment uses a phase plate to shape the intensity profile of the IR in focus (42; 43; 44) and measure the harmonic wavefronts using the SWORD technique (spectral wavefront optical reconstruction by diffraction) (45).

## 4.1 Knife-edge experiment

This chapter goes through the details of the experiment, analysis and simulations that Paper I is based on.

### Simulation

The simulation is based on a Gaussian description of the IR and the harmonic beam, as well as the equations coming from the analytical expression of the dipole phase (Equations 19, 4a and 4b).

To define the IR beam, the waist size and peak intensity have to be known. These parameters were not measured in the experiment but estimated. The beam width before focusing was measured to be 38 mm in diameter. The iris between the DM and the focusing mirror had an opening of approximately 20 mm in diameter. Doing a simulation of a truncated beam, the beam waist radius at focus is about 350 $\mu$m, which is used in the simulation. The IR was assumed to be Gaussian even though an iris was used.

The peak intensity was chosen to be $I_0 = 1.5 \times 10^{14}$ W/cm$^2$. This is within the generating window where harmonics have reached the plateau (first dashed line in Figure 6) and where the number of free electrons in the medium does not ruin phase matching (the second line in Figure 6). Figure 6 was calculated for a 40 fs, 800 nm pulse in argon. The dashed lines are obtained for the 23$^{\text{rd}}$ harmonic using the time-dependent Schrödinger equation (TDSE) (46).

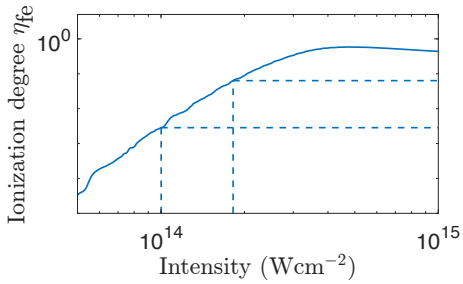


**Figure 6:** Ionization degree for harmonic 23 as a function of laser intensity, for a driving laser with 40 fs pulse duration and 800 nm central wavelength, calculated using TDSE.

The focusing, done in the experiment by a combination of the DM and the focusing mirror, was simplified in the simulation with only one focusing element with a varying focal length. The slightly varying waist size and Rayleigh length for different focal positions were accounted for.

Inserting the beam properties of the IR into Equations 19, 4a and 4b, those of the generated harmonics were obtained. To get the properties of the refocused beam, Equations 7 and 8 were used with a focal length of 16.5 mm and the results are shown in Figure 7, where $\Delta Z$ is the distance from the IR focus to the generation position. Only the short trajectory is shown since it is the most dominant trajectory in the experiment presented in this thesis.

As can be seen in Figure 7 (a), the harmonic focal positions are more spread out for negative generation positions. That is because the curvature from the dipole phase is always divergent while the curvature from the IR is going from convergent to divergent through the focus. Generating before the focus, the wavefront is the sum of a convergent and a divergent curvature, while generating after the focus, the curvature is only divergent.

The effect from the dipole phase is stronger for higher order harmonics. In Figure 7 (a) the 23$^{\text{rd}}$ and 25$^{\text{th}}$ harmonic always have a negative focus position, which means that they are always generated with a divergent curvature. The wavefront contribution from the dipole phase is always stronger than the IR wavefront. The 11$^{\text{th}}$ harmonic is less affected by the dipole phase wavefront contribution and therefore has a wavefront going from convergent to divergent in the same manner as the IR wavefront.

For harmonic 11 to 21, the maximum waist size coincides with the generation positions at which the curves are crossing zero, as seen in Figure 7 (a) and (b). This is when the harmonic has its waist at the generation.

Since the harmonics are never generated so that their focal positions coincide,

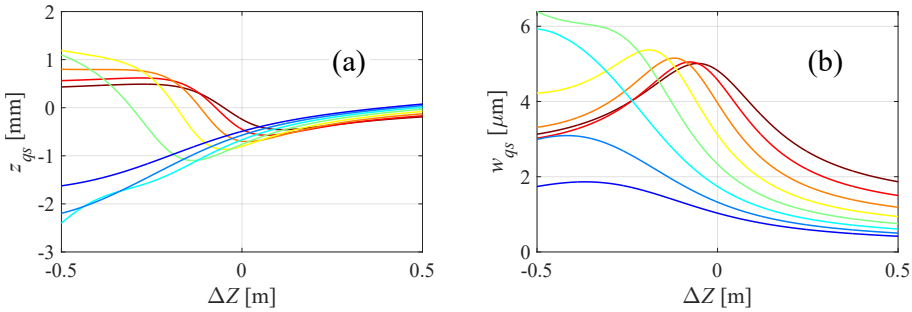


**Figure 7:** Simulated focus position relative to the refocused IR (a) for harmonic 11 (red) to 25 (blue), for the short trajectory, as a function of generation position $\Delta Z$, for a driving laser centre at 800 nm and a peak intensity of $1.5 \times 10^{14}$ W/cm$^2$. Waist size (b) for the same harmonics as a function of generation position. This simulation includes the varying waist size of the IR.

the refocused beam will always be spread out along the optical axis. This has consequences on both the temporal structure and the intensity, as discussed further down.

Figure 4 in Paper I shows the simulated focus position both without (a,b) and with (c,d) the dipole phase, for both the generation chamber and the refocused beam. The simulated waists are also shown in (e,f). The dashed lines in (d,f) is including the varying waist size when the focal length changes. This has a small effect on the focusing properties.

### Experimental method

To measure the individual harmonic focus positions a knife-edge was used together with the spectrometer. A sketch of the setup is shown in Figure 8. By inserting a knife along the horizontal axis ($x_k$), the diffraction of the knife for each harmonic could be analyzed with the spectrometer. A knife was mounted on a motorized stage that could move both along the propagation axis ($z_k$) and the horizontal transverse axis ($x_k$). The focus was characterized using two different methods, where the second one turned out to be more successful since it required fewer scans and did not rely on the motor step size resolution.

The first method is based on the idea that if the knife is inserted before the focus, its shadow appears on the opposite side, at the MCP. If the knife is placed after the focus it appears on the same side. By inserting the knife at many positions around the focus, the individual focus positions can be identified by finding at which position the shadow is changing side. Paper I shows the principle of this method, where, in Figure 2 (c), lower-order harmonics and higher-order harmonics have the knife-edge shadow at different sides.

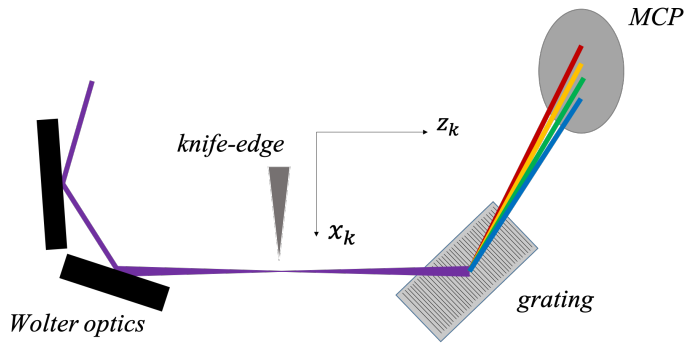


**Figure 8:** Setup for the knife-edge experiment. The XUV beam (purple) is focused after the Wolter optics. A knife that can be moved in the $x_k$- and $z_k$-direction is inserted into the beam. The beam is diffracted by a grating and detected by an MCP.

In the second method, the knife is inserted outside the Rayleigh region at two positions before and two after the focus. Looking at the intensity as a function of knife insertion, the width can be extracted. By knowing the width at four positions, the focus position can be found through linear interpolation, as described under *Analysis*.

A detailed description of the second method will now be described. The knife was attached to a movable mount connected to servo actuators with sub-micron resolution. The knife was moved into the beam in the $x_k$-direction with a step size of 5 $\mu$m. This was repeated for four $z_k$-positions: -8.3, -4.3, 9.1, and 13.7 mm, where -8.3 mm and 13.7 mm were the maximum positions of the motor and the IR focus was around $z_k \approx 0$ mm. For each $x_k$ and $z_k$ the harmonic spectrum, averaged over 20 shots, was recorded.

To vary the generation position in relation to the IR focus position, the IR beam curvature was varied by the deformable mirror. This was controlled by applying a voltage, which was calibrated by using a leak of the focusing beam (see Folding cross in Figure 4). Using a camera along a rail the position of the IR focus was measured for different voltage settings on the DM. The result of this calibration was that 1 V $\approx$ 1 cm.

The knife-edge scan was repeated for 11 different IR focus positions going from 30 cm before to 20 cm after the gas cell. As a reference, the Rayleigh length of the IR is about 50 cm. However, since the effective focal length is varied the beam waist and Rayleigh length are varying slightly for different focus positions.

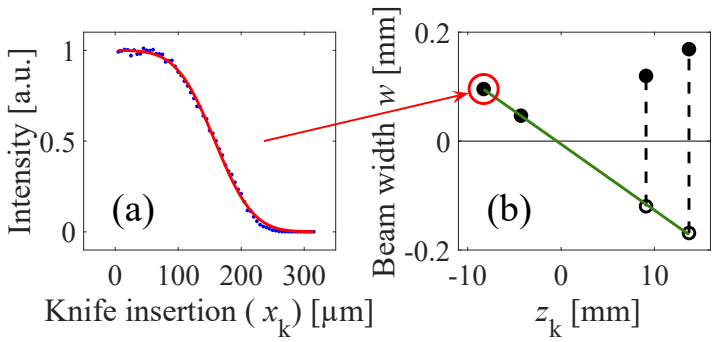


**Figure 9:** Schematic representation of the knife-edge technique. (a) intensity as a function of knife insertion is fitted to an errorfunction (red). The steepness of the errorfunction translates to a beam width in (b). After mirroring two beam widths (dashed black), a linear fit is performed (green) and the focus is found where this fit crosses zero.

## Analysis

Assuming a Gaussian beam, the harmonic intensity as a function of knife insertion should be the integral of a Gaussian, that is the normalized error function $f(x_\mathrm{k}) = \{\mathrm{erf}[b(x_\mathrm{k} - c)] + 1\}/2$. The experimental data were fitted to this error function as seen Figure 9 (a), for harmonic order 21 and the IR focus 5 cm after the gas cell. The beam width was determined from the fitting parameter $b$ that is related to the beam width as $w_q = \sqrt{2}/b$. After mirroring the two last beam widths, the focus position was found as the interaction of a linear fit to the beam width as a function of $z_k$ with zero, as shown in Figure 9 (b). The standard deviation of this fit was later used as an error bar after converting it to an error along $z_k$.

The measurements show that the harmonic focus positions are spread out, especially when the generation medium is located before the IR focus as seen in Figure 10. The dashed line shows the result from the simulation, which is in good agreement with the experimental data. Measurements presented in Paper I, Figure 5, show that the harmonic focus positions are closer to each other when the generation gas is after the focus.

The slope of the linear fit gives the divergence. Assuming an ideal Gaussian beam (i.e. $\mathbb{M}^2 = 1$), the beam waist is given by $w_{0,q} = \lambda/\pi\theta_{0,q}$. This can also be considered a lower limit to the beam waist since a non-ideal Gaussian beam would always have a larger waist for a given divergence. Having the focus position and the waist size, and assuming a Gaussian beam, the harmonic beam is fully defined.

Before each scan, a reference spectrum was taken, in order to get the beam width at the spectrometer. Knowing the distance from the focus to the spectrometer

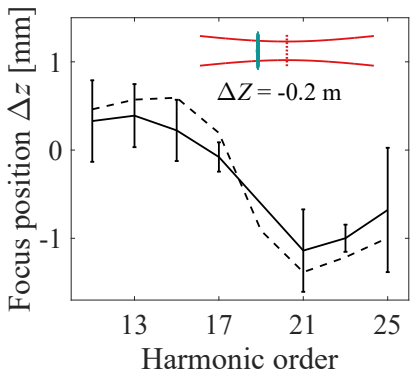


**Figure 10:** Experimental (solid) and simulated (dashed) harmonic focus position when the generation gas is 20 cm before the IR focus. The errorbars are calculated from the standard deviation from the linear fit.

(839 mm), the divergence could be calculated and be compared to that obtained by our knife-edge measurement. The waists from both methods are shown in Figure 11, where the solid curves come from the width at the spectrometer and the dashed from the linear fit described in Figure 9. The waist is shown for each harmonic going from 11 (dark red) to 25 (dark blue), as a function of generation position $\Delta Z = Z_m - Z_0$, where $Z_m$ is the medium position and $Z_0$ is the IR focus position. This comparison strengthens the validity of our measurement.

### Pulse Duration and Intensity

An estimation of the temporal structure and intensity of the attosecond pulses in the train was done based on the measured focus positions and estimated waist sizes of the high-order harmonics. The electric field as a function of time, $t$, $z$, and $\rho$ is given by

$$E(t,\rho,z) = \sum_q \sqrt{I_q(t,\rho,z)}\exp\Big(iq\omega t + i\phi_q(t,\rho,z)\Big), \tag{20}$$

where $I_q(t,\rho,z)$ is the intensity and $\phi_q(t,\rho,z)$ is the phase of the $q^{th}$ harmonic. The intensity is calculated by taking the absolute square of the amplitude in Equation 2. Since the waist and width are determined from our measurement, there is only one unknown in this equation, which is the relative intensity of the different harmonics, $I_{0,q} = |A_{0,q}|^2$. By integrating a reference spectrum the relative power, $P_q$, was determined. The power of a Gaussian beam can be expressed as, $P \propto I_0 w_0^2$, which gives the relative peak intensities, $I_{0,q} \propto P_q/w_{0,q}^2$.

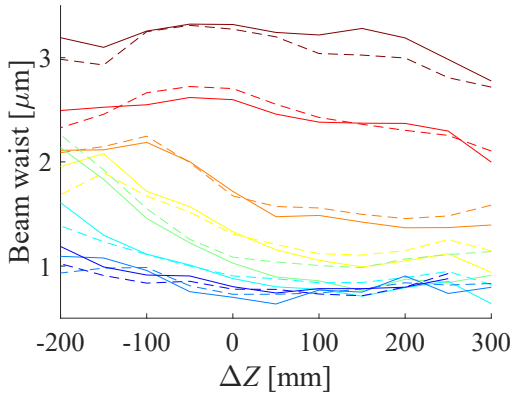


**Figure 11:** Harmonic beam waist determined from the width at the spectrometer (solid) and form the linear fit described with Figure 9 (dashed) as a function of generation position $\Delta Z$, for harmonic 11 (dark red) to 25 (dark blue).

The phase was not measured but instead assumed to be the sum of the dipole phase and the Gouy phase, given by Equations 15 and 3c. Including this into Equation 20, for different generation positions, a four-dimensional, $I(\Delta Z, t, \rho, z)$, matrix is produced. Different information can be extracted, for example, the on-axis intensity as a function of $z$. It is determined by setting $\rho = 0$ and extracting the maximum intensity among all $t$-values, for each $z$.

Figure 7(d) in Paper I shows the on-axis attosecond pulse train intensity along the propagation axis ($\Delta z$) as a function of the generation position ($\Delta Z$). With each curve is also the individual harmonic on-axis intensities multiplied by 2, plotted. In the Intensity-$\Delta Z$ plane, the peak intensity is shown in green and the normalized yield in red. The maximum intensity is achieved when the generation gas is in the focus or slightly after. The reason for this can be explained by comparing Figure 7(e,f,g) in Paper I. Generating 150 mm before the IR focus (e), the focus is spread out along the propagation axis. Generating 150 mm after the IR focus (g), the focus is fairly compact but the intensity is low due to the low yield. Therefore, the optimum is found somewhere in between, where the yield is high and the focus is not too spread out.

## 4.2 Focus control by IR shaping

In this section, the theory and experimental results of the SWORD measurements will be presented.

Equation 15 shows that the dipole phase depends on the order and on the IR intensity. This implies that the radially varying intensity translates into a

radially varying phase, in other words, a curved wavefront, that differs for each harmonic. If the intensity profile of the IR would be constant in the radial direction, i.e. a flat-top beam, this effect would disappear. The wavefront of the harmonics would only be affected by the wavefront of the IR. In this experiment, we shape the intensity profile of the IR to a super Gaussian, using a phase plate.

### Shaping the IR

The intensity profile of the IR was shaped by putting an anti-reflective coated $SiO_2$ phase plate into the beam that adds a $\pi$ phase shift to an inner disc of the beam, with a diameter of 20 mm. The total beam is then the sum of the inner beam and the annular outer beam, which are out of phase with each other. Next to the phase plate is an iris. By opening and closing the iris, the contribution from the annular beam is controlled. In the focus, the two beams interfere destructively which makes the intensity from the centre to be redistributed to the outer part of the beam creating a super Gaussian (42; 43; 44), as seen in the measured profile shown in Figure 12. It shows the intensity profile (blue) of the IR for different iris diameters, going from 20 mm to 27 mm, compared to the reference (red) that is the 20 mm iris diameter. The intensity profile was measured on the beam that leaks out from the folding mirror.

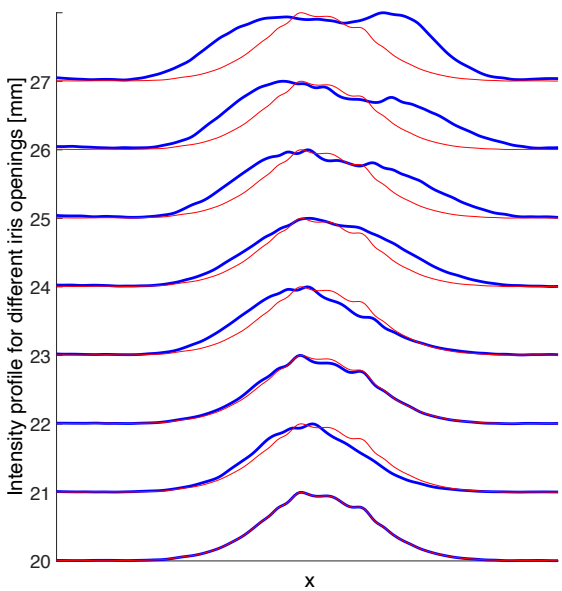


**Figure 12:** IR intensity profile in focus (blue) after it being shaped by the phase plate and different iris openings. The red curve shows the reference profile, i.e. when the iris has the same size as the inner disc of the phase plate and the IR is considered a Gaussian beam.

In the rest of this section, the effect of using the shaped and Gaussian beam for HHG will be compared. This refers to the 25 mm and 20 mm opened iris. The focus of the Gaussian beam is always placed at the generation cell. In addition to the spatial shape, the shaped beam has a lower peak intensity and wider waist than the Gaussian beam.

### Harmonic beam width

The harmonic beam widths were compared for the shaped and Gaussian IR by measuring the full width at half maximum (FWHM) of the beam profile at the MCP of the spectrometer. This was done while varying the laser energy with the attenuator. Figure 13 shows the FWHM of harmonic 11 to 19 generated with a super Gaussian (dashed) and Gaussian (solid) beam. The harmonics generated with a Gaussian beam are always larger and increase with laser intensity compared with those generated with the super Gaussian beam that are smaller and rather constant with laser energy.

Harmonics that are generated from the short trajectory, using a Gaussian IR with the focus centred at the generation medium, have a radius of curvature that is proportional to the peak intensity of the IR, as seen in Equation 19. Assuming a constant width at the generation position, the waist size will decrease when $R$ increases. This leads to an increased divergence and a larger beam width at the spectrometer. On the other hand, harmonics generated with a perfect flat top

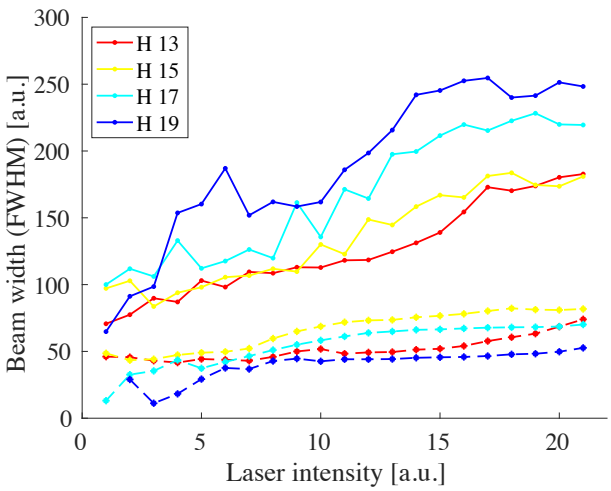


**Figure 13:** Harmonic beam widths at the spectrometer as a function of laser energy, generated with a Gaussian (solid) and shaped (dashed) IR beam.

IR do not have a wavefront contribution from the dipole phase and are therefore not affected by the peak intensity.

The cut-off harmonic of the shaped IR beam is around 19. The Gaussian beam has a higher cut-off due to its higher peak intensity, but only up to harmonic 19 is shown in this comparison.

### SWORD measurements

To do a more detailed study of how the harmonics are affected by the IR intensity profile, the SWORD technique was used to measure the radius of curvature of the harmonic wavefronts. The principle of the SWORD technique is to probe a small section of the wavefront with a narrow slit (45). The slit generates a diffraction pattern on the detector, which centre depends on the wavefront tilt, as sketched in Figure 14. By recording the diffraction pattern while scanning the slit position transverse over the beam, the radius of curvature can be calculated.

For a slit position, $z_i$, the centre of the diffraction pattern at the detector is positioned at

$$y_i = z_i + \frac{z_i}{R} d, \tag{21}$$

from the propagation axis, where $R$ is the radius of curvature and $d$ is the distance between the slit and the detector, as shown in Figure 14.

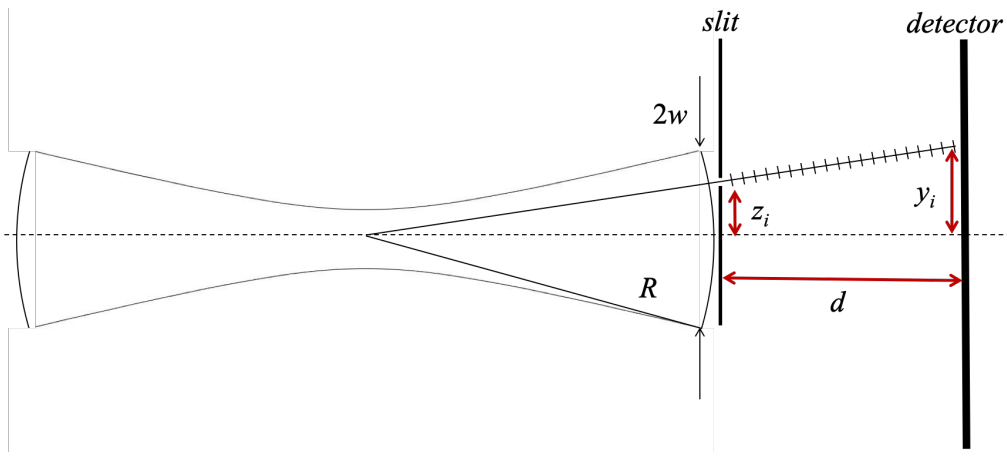


**Figure 14:** The principle of the SWORD technique, measuring the radius of curvature, $R$, and beam width, $w$, of a laser beam. The wavefront at the vertical slit position, $z_i$, has a tilt that determines the centre of the diffraction pattern, $y_i$, at the detector, placed at a distance $d$ from the slit.

In this experiment, a vertical slit, with a 120 $\mu$m width, was placed approximately 13 cm after the refocused XUV beam on a movable mount. This mount was controlled by a servo-actuator with sub-micron resolution (same as used in the knife-edge experiment). The slit was scanned over the beam in steps of 100 $\mu$m. For each slit position, the spectrum was recorded.

The beam width at the plane of the slit can also be determined by integrating the intensity at the detector for each slit position. The intensity profile is then fitted to a Gaussian function and the width can be determined. Knowing the width and the radius of curvature of the wavefront, the waist and focus position can be determined with Equations 4a and 4b.

## Results

We present two series of measurements, performed using a high-pressure jet and a 1 cm long cell for generation. The measurements were done on two different days. The DM voltage was tuned so that the intensity profile overlapped with the centre of the gas medium. Figure 15 shows the focus position (a) and waist (c) of harmonic 11 to 19 generated with the shaped (b) and Gaussian (d) beam. The solid (dashed) lines correspond to generation with the jet (cell). The focus positions are relative to that of harmonic 15.

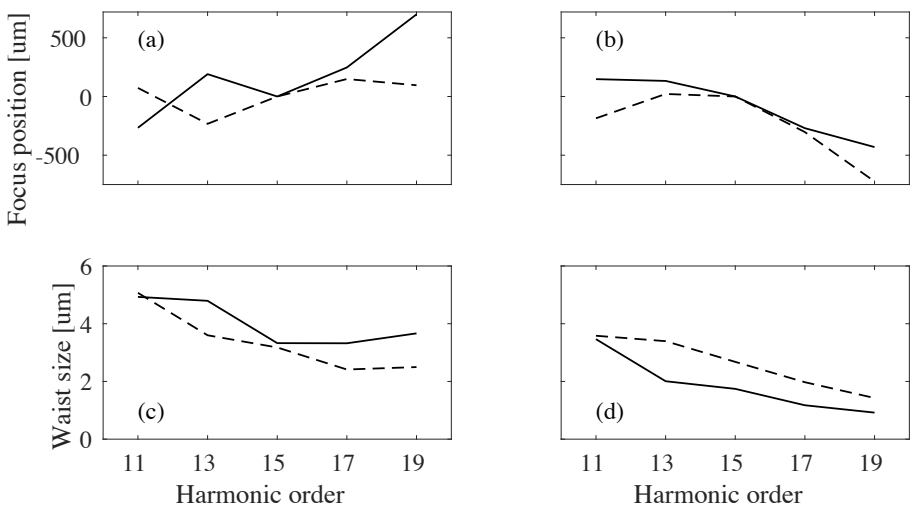


**Figure 15:** Relative focus positions and waist size for harmonic 11 to 19 generated with a shaped IR beam (a) and (c), and Gaussian beam (b) and (d). The solid lines are the results from using the jet and dashed lines from using the cell.

The lower order harmonics are focused before the higher order harmonics when generated with the shaped IR beam, while the opposite is observed with the Gaussian beam. The maximum separation of the focus positions is similar for the two cases. The harmonic waist size obtained with the shaped IR (Figure 15(c)) is larger than with the Gaussian IR (Figure 15(d)). That could be seen already in Figure 13, where the harmonics generated with the shaped IR had a smaller beam width in the far-field. This implies larger waist sizes than those generated with a Gaussian beam.

From the measured waist sizes and focus positions of the jet experiment, harmonic amplitudes were estimated assuming Gaussian beams and shown in Figure 16 for the shaped (a) and Gaussian (b) beam. The amplitudes are normalized to the highest amplitude in each case. The larger widths in (a) make the harmonics more overlapped even if their focus positions are equally spread out as in (b). This also affects the temporal structure along the propagation axis as seen in Figure 16 for the shaped (c) and Gaussian (d) beam. In Figure 16 (c)

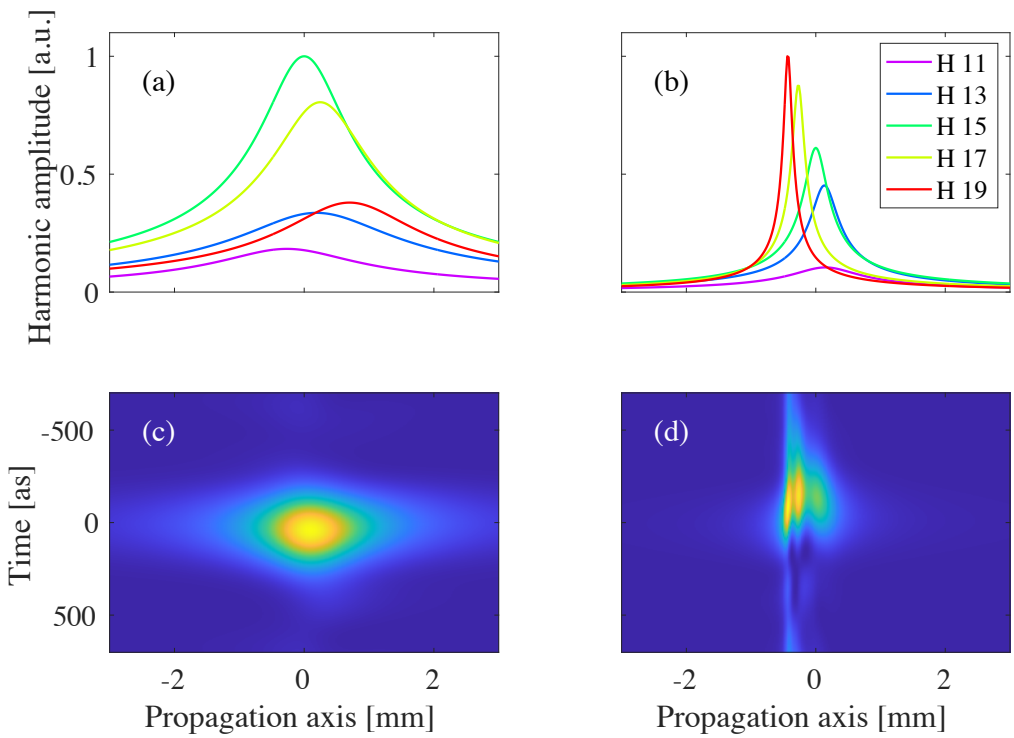


**Figure 16:** Harmonic amplitudes along the propagation axis generated with the jet and shaped IR beam (a) and Gaussian beam (b). The amplitudes are normalized to the maximum amplitude among all harmonics. The temporal structure is calculated with inverse Fourier transform at each position along the propagation axis, assuming the phase is given by the Gouy phase.

the intensity has a clear peak along the propagation axis while in (d) the focus is separated into several peaks. These images have been created in the same way as in the knife-edge experiment, using Equation 20 as described in Section 4.1, but without including the attochirp, which does not make a big difference. The results from the harmonics generated with the cell look very similar.

Due to the more overlapped harmonics from the shaped IR, the pulse duration does not increase so much in the focus. In the focus, the pulse duration has increased by 16% from the asymptotic value far away from the focus. In the case of the Gaussian IR it increases by 69%.

Generating high-order harmonics with a super Gaussian IR beam has an effect on the focus properties of the harmonics. The larger waist size is mostly an effect of the increased waist size of the IR. However, it is not only the waist that is affected but also the order dependent wavefront due to different tilts in Figure 15 (a) and (b). Possibly an intensity profile that is somewhere in between the super Gaussian and the Gaussian will generate harmonics with overlapping focus positions. The chromatic aberration and temporal structure in the focus are improved by using a super Gaussian IR beam. Due to the lower peak intensity in a super Gaussian compared to a Gaussian with the same energy, the cut-off harmonic is lower and the total XUV intensity goes down. This has to be compensated for with higher pulse energy.

# 5 RABBIT measurements

RABBIT (reconstruction of attosecond beating by interference of two-photon transition) is an interferometric technique that can be used to both characterize the attosecond pulse train (47) but also the photoionization process itself (48). In Paper II RABBIT was applied to the complete characterization of the photoionization of neon in the $2p^6$ shell.

RABBIT is a pump-probe technique where a combination of the APT and IR ionizes a gas. In the photon picture, it can be understood as a harmonic photon is absorbed and then an IR photon is either absorbed or emitted, keeping in mind that it is a direct process. This leads to an electron kinetic energy spectrum consisting of harmonic (H) and sideband (SB) peaks as shown in Figure 17 (modified from Paper II). The arrows show the absorption of harmonic (purple) and absorption (up) and emission (down) of IR (red) photons.

The spectrum is shown as a function of delay between the attosecond pulse train and the IR pulse. Due to the interference of two quantum paths leading to the same final state (absorption of harmonic plus one IR photon, absorption of the next harmonic plus emission of one IR photon) the spectrum oscillates with a frequency of $2\omega_{IR}$, where $\omega_{IR}$ is the angular frequency of the IR. The oscillation of the sideband has a phase, $\Delta\phi = \Delta\phi_{XUV} + \Delta\phi_A$, where $\Delta\phi_{XUV}$ is the phase difference between two harmonics and $\Delta\phi_A$ is a contribution from

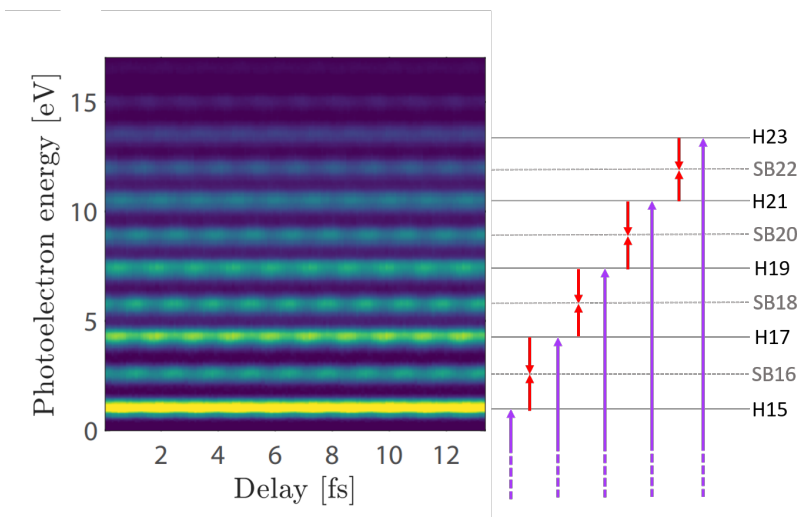


**Figure 17:** Angle integrated photoelectron spectrum in neon as a function of delay. Purple arrows symbolises the absorption of the different harmonic orders. Red arrows symbolises the absorption or emission of IR photons, forming sidebands (SB). The figure is modified from Paper II.

photoionization. $\Delta\phi_{XUV}/2\omega_{IR}$ represent the group delay of the attosecond pulses and the attosecond pulse train can be reconstructed in the temporal domain through inverse Fourier transform from the spectral amplitude and this phase. $\Delta\phi_A$ can be used to gain information about the photoionization process.

Thanks to the angular resolution of the DVMIS, angle-resolved RABBIT could be done. In a photoionization process, the created electron wavepacket is a sum of partial waves that have different angular momenta. The angular resolution gives information on the relative strength of these channels.

In Paper II we are studying the photoionization of the $2p^6$ shell in neon. As shown in Figure 1 in Paper II, the electron can be ionized through two different channels, ending up in s- or d-states. The absorption (or emission from the next harmonic) of an IR from these two states leads to the emission of p- or f-states.

As can be seen in Figure 2c in Paper II, the sideband intensity depends both on angle and delay. That is a result of the interference between the different channels leading to that sideband. By expressing this intensity as a sum of the different channels and performing a global fit to the data, the amplitude and phase of the two single-photon ionization channels were found.

# 6 Outlook

This thesis has focused on the beam properties of high-order harmonics and how those are affected by the generation itself. Understanding the generation process is crucial in order to control the XUV radiation. This research has deepened the understanding of how the focus can be optimized. That is one step towards more controlled experiments with HHG. This kind of research is for example important for the new extreme light infrastructure (ELI) that are building the next generation HHG sources ([49]). In addition, an application to photoionization has been presented.

## 6.1 Further focus characterization

Both the knife-edge and SWORD experiments are measuring the beam along one dimension. If more dimensions had been measured more information would have been accessible, such as the individual harmonic astigmatism. The knife-edge technique, used in our experiment to map out each harmonic focus position, can be used in any dimension. What is recorded is only the intensity as a function of knife insertion. Astigmatism could be measured by doing a knife-edge measurement along and perpendicular to the direction of the astigmatism axis.

To estimate the harmonic beam waists, ideal Gaussian beams have been assumed. The harmonic beams could instead be described as a Gaussian beam with a quality factor $\mathbb{M}^2$, which is probably closer to reality. An estimation of this factor could be done with a knife-edge scan at more positions along the propagation axis including both closer to the focus and far away.

## 6.2 Applications

Optimizing the focus is important in all applications that require short pulse duration and/or high peak intensity. One application that requires both of these is XUV-XUV pump-probe experiments with attosecond resolution. The setup needed for such an experiment is installed, so what is left is to have a good focus and good overlap with the atomic or molecular jet. This is not a trivial problem in the current setup. The jet is positioned where the medium is imaged and that is not necessarily where the harmonics are focused. Their focus positions will also vary when the IR focus position moves. This cannot be compensated for by the Wolter optics while keeping the aberration correction.

One solution would be to have a movable jet. That configuration would also enable us to take advantage of the spatially separated harmonic foci, using different parts of the spectrum by simply moving the jet along the propagation axis. This could also be a way of characterizing the focus.

# 7 References


[1] J. von Fraunhofer, "Bestimmung des brechungs und des farbenzerstreuungs - vermögens verschiedener glasarten, in bezug auf die vervollkommnung achromatischer fernröhre," *Denkschriften der Königlichen Akademie der Wissenschaften zu München*, vol. 5, pp. 193–226, 1814 - 1815.

[2] A. McPherson, G. Gibson, H. Jara, U. Johann, T. S. Luk, I. A. McIntyre, K. Boyer, and C. K. Rhodes, "Studies of multiphoton production of vacuum-ultraviolet radiation in the rare gases," *Journal of the Optical Society of America B*, vol. 4, pp. 595–601, 1987.

[3] M. Ferray, A. L'Huillier, X. Li, L. Lompre, G. Mainfray, and C. Manus, "Multiple-harmonic conversion of 1064 nm radiation in rare gases," *J. Phys. B*, vol. 21, pp. L31–L35, 1988.

[4] P. . M. Paul, E. Toma, P. Breger, G. Mullot, F. Augé, P. Balcou, H. Muller, and P. Agostini, "Observation of a train of attosecond pulses from high harmonic generation," *Science*, vol. 292, pp. 1689–1692, jun 2001.

[5] M. Schultze, M. Fieß, N. Karpowicz, J. Gagnon, M. Korbman, M. Hofstetter, S. Neppl, A. L. Cavalieri, Y. Komninos, T. Mercouris, C. A. Nicolaides, R. Pazourek, S. Nagele, J. Feist, J. Burgdörfer, A. M. Azzeer, R. Ernstorfer, R. Kienberger, U. Kleineberg, E. Goulielmakis, F. Krausz, and V. S. Yakovlev, "Delay in photoemission," *Science*, vol. 328, pp. 1658–1662, 2010.

[6] M. Isinger, R. J. Squibb, D. Busto, S. Zhong, A. Harth, D. Kroon, S. Nandi, C. L. Arnold, M. Miranda, J. M. Dahlström, E. Lindroth, R. Feifel, M. Gisselbrecht, and A. L'Huillier, "Photoionization in the time and frequency domain," *Science*, vol. 358, no. 6365, pp. 893–896, 2017.

[7] F. Calegari, D. Ayuso, A. Trabattoni, L. Belshaw, S. De Camillis, S. Anumula, F. Frassetto, L. Poletto, A. Palacios, P. Decleva, J. B. Greenwood, F. Martin, and M. Nisoli, "Ultrafast electron dynamics in phenylalanine initiated by attosecond pulses," *Science*, vol. 346, no. 6207, pp. 336–339, 2014.

[8] P. M. Kraus, B. Mignolet, D. Baykusheva, A. Rupenyan, L. Horný, E. F. Penka, G. Grassi, O. I. Tolstikhin, J. Schneider, F. Jensen, L. B. Madsen, A. D. Bandrauk, F. Remacle, and H. J. Wörner, "Measurement and laser control of attosecond charge migration in ionized iodoacetylene," *Science*, vol. 350, no. 6262, pp. 790–795, 2015.

[9] M. Drescher, M. Hentschel, R. Kienberger, M. Uiberacker, V. Yakovlev, A. Scrinzi, T. Westerwalbesloh, U. Kleineberg, U. Heinzmann, and F. Krausz, "Time-resolved atomic inner-shell spectroscopy," *Nature*, vol. 419, p. 803, 2002.

[10] P. Agostini and L. F. DiMauro, "The physics of attosecond light pulses," *Rep. Prog. Phys*, vol. 67, p. 813, 2004.

[11] J. Tate, T. Auguste, H. G. Muller, P. Salieres, P. Agostini, and L. F. DiMauro, "Scaling of Wave-Packet Dynamics in an Intense Midinfrared Field," *Phys. Rev. Lett.*, vol. 98, p. 013901, 2007.

[12] A. D. Shiner, C. Trallero-Herrero, N. Kajumba, H.-C. Bandulet, D. Comtois, F. Légaré, M. Giguère, J.-C. Kieffer, P. B. Corkum, and D. M. Villeneuve, "Wavelength scaling of high harmonic generation efficiency," *Phys. Rev. Lett.*, vol. 103, p. 073902, Aug 2009.

[13] P. A. Carpeggiani, P. Tzallas, A. Palacios, D. Gray, F. Martín, and D. Charalambidis, "Disclosing intrinsic molecular dynamics on the 1-fs scale through extreme-ultraviolet pump-probe measurements," *Phys. Rev. A*, vol. 89, p. 023420, Feb 2014.

[14] P. Tzallas, D. Charalambidis, N. A. Papadogiannis, K. Witte, and G. D. Tsakiris, "Direct observation of attosecond light bunching," *Nature*, vol. 426, p. 267, 2003.

[15] Y. Nabekawa, H. Hasegawa, E. J. Takahashi, and K. Midorikawa, "Production of Doubly Charged Helium Ions by Two-Photon Absorption of an Intense Sub-10-fs Soft X-Ray Pulse at 42 eV Photon Energy," *Phys. Rev. Lett.*, vol. 94, p. 043001, 2005.

[16] C. M. Heyl, H. Coudert-Alteirac, M. Miranda, M. Louisy, K. Kovacs, V. Tosa, E. Balogh, K. Varjú, A. L,ÄôHuillier, A. Couairon, and C. L. Arnold, "Scale-invariant nonlinear optics in gases," *Optica*, vol. 3, pp. 75–81, jan 2016.

[17] B. Manschwetus, L. Rading, F. Campi, S. Maclot, H. Coudert-Alteirac, J. Lahl, H. Wikmark, P. Rudawski, C. M. Heyl, B. Farkas, T. Mohamed, A. L'Huillier, and P. Johnsson, "Two-photon double ionization of neon using an intense attosecond pulse train," *Phys. Rev. A*, vol. 93, p. 061402, Jun 2016.

[18] B. E. A. Saleh and M. C. Teich, *Fundamentals of Photonics*. John Wiley and Sons, 2007.

[19] P. Corkum, "Plasma perspective on strong-field multiphoton ionization," *Phys. Rev. Lett.*, vol. 71, p. 1994, 1993.

[20] K. C. Kulander, K. J. Schafer, and J. L. Krause, "Dynamics of short-pulse excitation, ionization and harmonic conversion," in *Super-Intense Laser-Atom Physics*, Plenum Press, New York, 1993.

[21] M. Lewenstein, K. C. Kulander, K. J. Schafer, and P. H. Bucksbaum, "Rings in above-threshold ionization: A quasiclassical analysis," *Phys. Rev. A*, vol. 51, p. 1495, 1995.

[22] C. Guo, A. Harth, S. Carlström, Y.-C. Cheng, S. Mikaelsson, E. Mårsell, C. Heyl, M. Miranda, M. Gisselbrecht, M. B. Gaarde, K. J. Schafer, A. Mikkelsen, J. Mauritsson, C. L. Arnold, and A. L'Huillier, "Phase control of attosecond pulses in a train," *J. Phys. B: At., Mol. Opt. Phys.*, vol. 51, p. 034006, jan 2018.

[23] H. Wikmark, C. Guo, J. Vogelsang, P. W. Smorenburg, H. Coudert-Alteirac, J. Lahl, J. Peschel, P. Rudawski, H. Dacasa, S. Carlström, S. Maclot, M. B. Gaarde, P. Johnsson, C. L. Arnold, and A. L'Huillier, "Spatiotemporal coupling of attosecond pulses," *Proceedings of the National Academy of Sciences*, 2019.

[24] C. Hernández-García, J. San Román, L. Plaja, and A. Picón, "Quantum-path signatures in attosecond helical beams driven by optical vortices," *New Journal of Physics*, vol. 17, p. 093029, sep 2015.

[25] F. Catoire, A. Ferré, O. Hort, A. Dubrouil, L. Quintard, D. Descamps, S. Petit, F. Burgy, E. Mével, Y. Mairesse, and E. Constant, "Complex structure of spatially resolved high-order-harmonic spectra," *Physical Review A*, vol. 94, dec 2016.

[26] L. Rego, J. San Román, A. Picón, L. Plaja, and C. Hernández-García, "Nonperturbative twist in the generation of extreme-ultraviolet vortex beams," *Physical Review Letters*, vol. 117, oct 2016.

[27] J. A. Pérez-Hernández, L. Roso, and L. Plaja, "Harmonic generation beyond the strong-field approximation: the physics behind the short-wave-infrared scaling laws," *Optics Express*, vol. 17, p. 9891, may 2009.

[28] C. G. Durfee III, A. R. Rundquist, S. Backus, C. Herne, M. M. Murnane, and H. C. Kapteyn, "Phase matching of high-order harmonics in hollow waveguides," *Phys. Rev. Lett.*, vol. 83, p. 2187, 1999.

[29] P. Maine, D. Strickland, P. Bado, M. Pessot, and G. Mourou, "Generation of ultrahigh peak power pulses by chirped pulse amplification," *IEEE J. Quantum Electron.*, vol. 24, p. 398, 1988.

[30] B. C. Platt and R. Shack, "History and principles of Shack-Hartmann wavefront sensing," *Journal of Refractive Surgery*, vol. 17, pp. S573–S577, 2001.

[31] H. Wikmark, "A high-order harmonic pump-probe setup using annular-beam interferometers," 2016. MSc Thesis.

[32] H. Wikmark, *Spatial and temporal aspects of intense attosecond pulses for pump-probe experiments*. PhD thesis, Lund University, 2019.

[33] F. Campi, H. Coudert-Alteirac, M. Miranda, L. Rading, B. Manschwetus, P. Rudawski, A. L'Huillier, and P. Johnsson, "Design and test of a broadband split-and-delay unit for attosecond XUV-XUV pump-probe experiments," *Review of Scientific Instruments*, vol. 87, no. 2, p. 023106, 2016.

[34] U. Even, "Pulsed supersonic beams from high pressure source: Simulation results and experimental measurements," *Advances in Chemistry*, vol. 2014, pp. 1–11, aug 2014.

[35] H. Coudert-Alteirac, H. Dacasa, F. Campi, E. Kueny, B. Farkas, F. Brunner, S. Maclot, B. Manschwetus, H. Wikmark, J. Lahl, L. Rading, J. Peschel, B. Major, K. Varjú, G. Dovillaire, P. Zeitoun, P. Johnsson, A. L'Huillier, and P. Rudawski, "Micro-focusing of broadband high-order harmonic radiation by a double toroidal mirror," *Applied Sciences*, vol. 7, p. 1159, nov 2017.

[36] P. Mercère, P. Zeitoun, M. Idir, S. L. Pape, D. Douillet, X. Levecq, G. Dovillaire, S. Bucourt, K. A. Goldberg, P. P. Naulleau, and S. Rekawa, "Hartmann wave-front measurement at 13.4 nm with $\lambda_{EUV}/120$ accuracy," *Opt. Lett.*, vol. 28, pp. 1534–1536, Sep 2003.

[37] L. Montgomery Smith, D. R. Keefer, and S. Sudharsanan, "Abel inversion using transform techniques," *Journal of Quantitative Spectroscopy and Radiative Transfer*, vol. 39, pp. 367–373, may 1988.

[38] D. R. Austin, T. Witting, C. A. Arrell, F. Frank, A. S. Wyatt, J. P. Marangos, J. W. Tisch, and I. A. Walmsley, "Lateral shearing interferometry of high-harmonic wavefronts," *Optics Letters*, vol. 36, p. 1746, may 2011.

[39] E. Frumker, G. G. Paulus, H. Niikura, A. Naumov, D. M. Villeneuve, and P. B. Corkum, "Order-dependent structure of high harmonic wavefronts," *Optics Express*, vol. 20, p. 13870, jun 2012.

[40] D. T. Lloyd, K. O'Keeffe, and S. M. Hooker, "Complete spatial characterization of an optical wavefront using a variable-separation pinhole pair," *Opt. Lett.*, vol. 38, pp. 1173–1175, Apr 2013.

[41] L. Quintard, V. Strelkov, J. Vabek, O. Hort, A. Dubrouil, D. Descamps, F. Burgy, C. Péjot, E. Mével, F. Catoire, and E. Constant, "Optics-less focusing of XUV high-order harmonics," *Science Advances*, vol. 5, apr 2019.

[42] A. Dubrouil, Y. Mairesse, B. Fabre, D. Descamps, S. Petit, E. Mével, and E. Constant, "Controlling high harmonics generation by spatial shaping of high-energy femtosecond beam," *Optics Letters*, vol. 36, p. 2486, jun 2011.

[43] E. Constant, A. Dubrouil, O. Hort, S. Petit, D. Descamps, and E. Mével, "Spatial shaping of intense femtosecond beams for the generation of high-energy attosecond pulses," *Journal of Physics B*, vol. 45, no. 7, p. 074018, 2012.

[44] W. Boutu, T. Auguste, O. Boyko, I. Sola, P. Balcou, L. Binazon, O. Gobert, H. Merdji, C. Valentin, E. Constant, E. Mével, and B. Carré, "High-order-harmonic generation in gas with a flat-top laser beam," *Phys. Rev. A*, vol. 84, p. 063406, Dec 2011.

[45] E. Frumker, G. G. Paulus, H. Niikura, D. M. Villeneuve, and P. B. Corkum, "Frequency-resolved high-harmonic wavefront characterization," *Opt. Lett.*, vol. 34, pp. 3026–3028, Oct 2009.

[46] R. Weissenbilder, 2021. Private Communication.

[47] P. Paul, E. Toma, P. Breger, G. Mullot, F. Augé, P. Balcou, H. Muller, and P. Agostini, "Observation of a train of attosecond pulses from high harmonic generation," *Science*, vol. 292, p. 1689, 2001.

[48] K. Klünder, J. M. Dahlström, M. Gisselbrecht, T. Fordell, M. Swoboda, D. Guénot, P. Johnsson, J. Caillat, J. Mauritsson, A. Maquet, R. Taïeb, and A. L'Huillier, "Probing single-photon ionization on the attosecond time scale," *Phys. Rev. Lett.*, vol. 106, p. 143002, 2011.

[49] S. Kühn, M. Dumergue, S. Kahaly, S. Mondal, M. Füle, T. Csizmadia, B. Farkas, B. Major, Z. Várallyay, E. Cormier, M. Kalashnikov, F. Calegari, M. Devetta, F. Frassetto, E. Månsson, L. Poletto, S. Stagira, C. Vozzi, M. Nisoli, P. Rudawski, S. Maclot, F. Campi, H. Wikmark,

C. L. Arnold, C. M. Heyl, P. Johnsson, A. L'Huillier, R. Lopez-Martens, S. Haessler, M. Bocoum, F. Boehle, A. Vernier, G. Iaquaniello, E. Skantzakis, N. Papadakis, C. Kalpouzos, P. Tzallas, F. Lépine, D. Charalambidis, K. Varjú, K. Osvay, and G. Sansone, "The ELI-ALPS facility: the next generation of attosecond sources," *Journal of Physics B: Atomic, Molecular and Optical Physics*, vol. 50, p. 132002, jun 2017.

# Scientific publications

### Paper I: Focusing Properties of High-Order Harmonics

We measured the chromatic aberration of high order harmonics with a knife-edge technique. We compared the experimental data with simulations to explain that the order dependent properties originates from the generation process. I performed the experiment, analysed the data, did simulations and wrote the main part of the manuscript.

### Paper II: Complete characterization of multi-channel single photon ionization

We studied a multi-channel photoionization process using RABBIT. I prepared the experimental setup.